Eur. Phys. J. B **42**, 321–336 (2004)
DOI: 10.1140/epjb/e2004-00387-2

THE EUROPEAN PHYSICAL JOURNAL B

# Flux dynamics, superconducting, and normal state properties of $Gd(Ba_{2-x}Pr_x)Cu_3O_{7+\delta}$

M.R. Mohammadizadeh and M. Akhavan[a]

Magnet Research Laboratory (MRL), Department of Physics, Sharif University of Technology, P.O. Box 11365-9161, Tehran, Iran

Received 27 November 2003 / Received in final form 4 July 2004
Published online 23 December 2004 – 

**Abstract.** $Gd(Ba_{2-x}Pr_x)Cu_3O_{7+\delta}$ single phase polycrystalline samples with $0.0 \leq x \leq 1.0$ were investigated for structural, electronic and flux dynamics properties. Two-dimensional variable range hopping (VRH) is the dominant conduction mechanism in the normal state of the system. Pr doping strongly localizes the carriers in normal state, and finally causes the suppression of superconductivity. The effect of Pr substitution in 123 structure of HTSC at R or Ba sites is to increase the pseudogap temperature $T_s$, although, Pr at Ba sites has a stronger effect on the increase of $T_s$ and suppression of superconductivity. The magnetoresistance of the samples have been studied within thermally activated flux creep and the Ambegaokar and Halperin phase slip models. The derived critical current density, $H_{c2}(T)$, $H_{c2}(0)$, and superconducting coherence length $\xi$ show that the Pr doping, like weak links, decreases the vortex flux pinning energy. Our results imply that understanding the real suppression mechanism of superconductivity by Pr doping in HTSC is connected crucially to the exact position of Pr in the structure.

**PACS.** 74.72.Bk Y-based cuprates – 74.62.Dh Effects of crystal defects, doping and substitution – 74.62.Bf Effects of material synthesis, crystal structure, and chemical composition – 74.25.Fy Transport properties (electric and thermal conductivity, thermoelectric effects, etc.) – 74.25.Op Mixed states, critical fields, and surface sheaths

## Introduction

One of the interesting subjects in high temperature superconductors (HTSC) is the insulating behavior of $PrBa_2Cu_3O_{7-\delta}$(Pr-123) in the orthorhombic phase. This is in contrast with the other $RBa_2Cu_3O_{7-\delta}$ (R-123) compound (R = Y and rare earth elements), which becomes a superconductor at about 90 K [1,2]. Different anomalous effects have been observed when Pr (or Pr with other elements like Ca [3]) is substituted in R-123, or in other HTSC families. Although many attempts have been made to explain the insulating behavior of Pr-123, some groups have recently reported observation of superconductivity in the powder [4], single crystal [5,6], polycrystalline [7], and Pr-123/Y-123 bilayer thin films [8] of this compound. Since these studies, the behaviour of Pr-123 has attracted much more attention, and the question is under what conditions, if ever, could Pr-123 compound become a superconductor? Recently, Akhavan has reviewed the effects of Pr substitution [9], and Pr/Ba mis-substitution in HTSCs [10].

There are metal-insulator transition (MIT) and superconductor-insulator transitions (SIT) observed with Pr doping in RPr-123 compounds. Different explanations for these effects in RPr-123 such as hole filling [11], pair breaking [12], and hybridization [13], the substitution of Pr at the Ba site ($Pr_{Ba}$) (mis-substitution effect) rather than at R sites have been proposed for the insulating behavior of Pr-123 [14]. This proposal seems relevant due to the nearly equivalent positions of R and Ba sites in the center of the imperfect R-123 perovskite structure, and the fact that superconductivity is suppressed in $R(Ba_{2-x}R'_x)Cu_3O_{7+\delta}$ compounds (R′ = rare earth, not necessarily the same atom as R) [15]. In this regard, by the Rietveld structural refinement, we have studied the possibility of Pr mis-substitution at Ba sites in $(Gd_{1-x}Pr_x)Ba_2Cu_3O_{7-\delta}$ compounds, concluding that the $Pr_{Ba}$ mis-substitution is not the main reason for suppression of superconductivity in the system [16]. In a more advanced approach, it is better to confirm the Rietveld structural refinements with the calculation of atomic valences, based on the bond valence sum (BVS) technique [17].

Moreover, the normal state of the high temperature cuprate superconductors shows many unusual properties, which are far from the standard Fermi liquid behavior. A typical anomalous property is the temperature dependence of the resistivity, which is linearly proportional to

[a] e-mail: akhavan@sharif.edu

the temperature $T$. This is in contrast with the $T^2$ dependence expected from Fermi liquid theory.

Another feature in HTSC is the so-called pseudogap behavior observed in the under-doped region near the Mott insulating phase, which is a frequency threshold for the strong excitation of spin and charge modes [18]. The pseudogap is a fundamental property of the under-doped copper oxides [19]. An explanation of the pseudogap phenomenon is regarded as one of the most important unresolved questions in the theory of superconductivity. The substitution of Pr at Ba sites instead of R sites, has also been studied in reference [20]. The substitution of Pr at Ba or R site has different effects on transport properties, which in turn, influences the psuedogap opening temperature. The evolution of pseudogap as a function of different impurity concentrations and its relation to superconductivity is an important step to elucidate the mechanism of superconductivity in HTSC.

Among different models for describing the charge transport in materials, the variable range hopping (VRH) conduction between localized states have been widely used for normal state of HTSC [21]. There are some reports, which show that VRH in three dimensions (3D-VRH) is a proper mechanism in the normal state conductivity of HTSC [22], as well as 2D-VRH [23], and Coulomb gap (CG) regime [24]. So, it is valuable to find an approach to explore the dominant conduction mechanism(s) in the normal state of HTSC.

Among transport properties, one of the most important physical quantities for a superconductor is its superconducting transition temperature variation upon application of the magnetic field [25]. The polycrystalline samples present a pronounced granular character that plays an important role in many of their properties. For instance, the resistive transition of these systems has the characteristic of a two-stage process [26]. At higher temperatures, superconductivity stabilizes in homogenous and mesoscopic regions of the sample i.e., grains, which is the pairing transition. At lower temperatures, close to $T_c(\rho = 0)$, a long-range superconducting state with zero resistance is achieved by means of a percolation like process that controls the activation of weak links between grains. Under applied magnetic field, the weak links are affected and therefore, the tail part dissipates in even small fields. In large magnetic fields, due to flux penetration inside the grains the onset part of transition will be broadened.

In this paper, regarding the $Gd(Ba_{2-x}Pr_x)Cu_3O_{7+\delta}$ compound, which is being investigated for the first time, the complete structural details are explained in Section 1. The transport, normal state conduction mechanism, and pseudogap are discussed in Section 2, and finally, magnetoresistance and flux dynamics in the mixed state are presented in Section 3.

## Experimental and computational details

$Gd(Ba_{2-x}Pr_x)Cu_3O_{7+\delta}$ (GdBaPr-123) single phase samples with $x = 0.00$, 0.05, 0.10, 0.15, 0.20, 0.25, 0.30, 0.35, 0.40, 0.50, 0.60, 0.80, and 1.00 were synthesized by the standard solid state reaction technique. In accordance with the procedures followed in our previous report [27], appropriate amounts of $Gd_2O_3$, $Pr_6O_{11}$, $BaCO_3$, and CuO powders with 99.9% purity were mixed, ground, and calcined at 840 °C for 24 h in an air atmosphere. Calcination was repeated twice with intermediate grinding. Then powders were reground, pressed into pellets, and annealed at 930 °C for 24 h in an oxygen atmosphere. The samples were cooled to 550 °C and retained under oxygen flow for 16 h. Finally, they were furnace cooled to room temperature. The oxygen content of samples has been determined by the iodometric titration technique with $\pm 0.03$ accuracy.

SEM measurements were made to determine the grain size and homogeneity of the samples using a JEOL-JXA-840 instrument. XRD measurements were performed using a Philips PW-3710 powder diffractometer with Cu $K_\alpha$ radiation and $\lambda = 1.5406$ Å at room temperature with a 0.02° step width and a 0.5 second step time. The XRD results were analyzed using the DBW3.2S-PC-9207 package [28] based on the Rietveld method [29]. In the refinement of up to 27 parameters, including the scale factor, cell parameters ($a, b$, and $c$), atomic coordinates, isotropic displacements (B), site occupation factors (N), and profile shape parameters were allowed to vary. The B of the oxygen atoms was fixed to 1.0 Å [30]. The background was refined and a Lorentzian profile function was used for all samples. The refinements were based on diffraction data in the range $5° \leq 2\theta \leq 120°$ containing 37 reflections from orthorhombic phase and 32 reflections from tetragonal phase. The accuracy of the lattice parameters for $a$ and $b$ are at least 0.0005 Å and for $c$ is 0.002 Å. The accuracy of N, B, and Z in the Rietveld refinements are at least 0.01, 0.4 Å, and 0.003 Å, respectively.

An ac four-probe method with $f = 33$ Hz was used for the conductivity measurements of the samples within the temperature range of 10 to 300 K. The size of the samples was about $8 \times 3 \times 2$ mm$^3$. The electrical contacts were attached to the long side of the samples by silver paste. A Lake Shore-330 temperature controller with two Pt-100 resistors was used for measuring and controlling the temperature to within $\pm 10$ mK. Different currents from 10 to 100 mA were applied in resistivity measurements. For the magnetoresistivity measurements, a dc magnetic field of maximum value 20 kOe was applied perpendicular to the current and surface of the samples.

## Results and discussion

### 1. Structural properties

The SEM micrographs of the samples show a homogenous granular structure with micrometer grain size. The measured mass densities of the samples decreases from 5.47 to 4.29 gr/cm$^3$ with increasing $x$. The mass density decreases by replacing the larger and lighter Ba atom with the smaller and heavier Pr atom in Gd-123 structure. In the same preparation conditions, the mass density should increase with increasing $x$, whereas it decreases. This

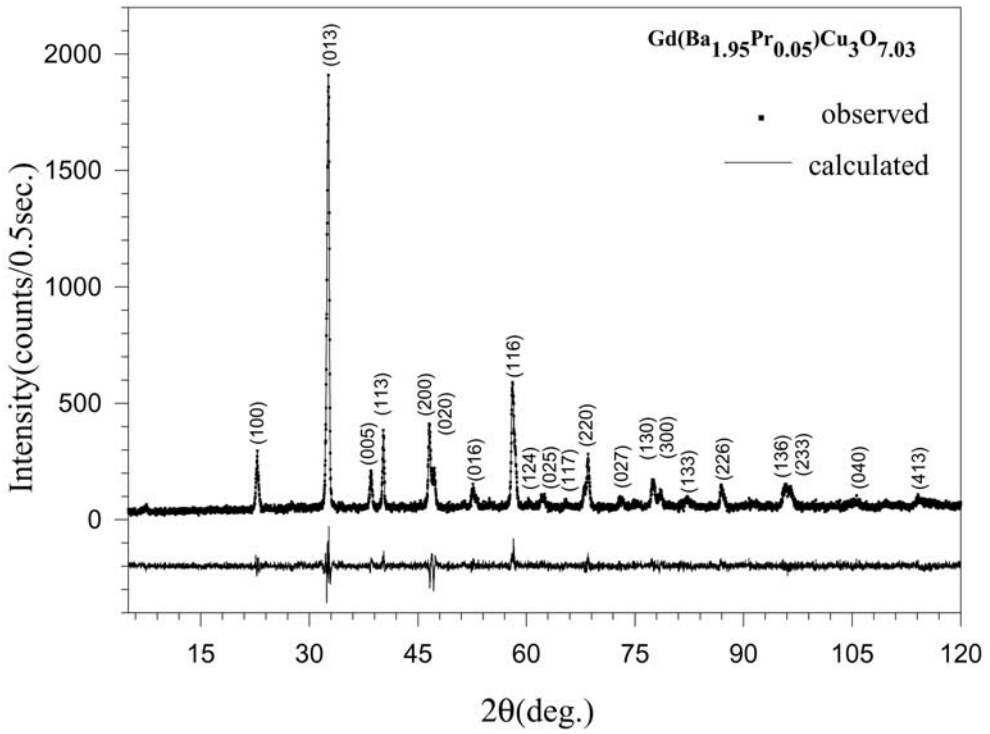


**Fig. 1.** The observed XRD pattern, the Rietveld refinement calculation, and their differences (at the bottom) for the $x = 0.05$ sample.

shows that Pr substitution increases the porosity of the samples, which in turn causes a decrease instead of an increase in the mass density with Pr doping.

Figure 1 shows a typical XRD pattern, Rietveld refinement result and their differences for $Gd(Ba_{1.95}Pr_{0.05})Cu_3O_{7.03}$ sample. It shows that within the XRD limitations, a single phase of 123 structure has been formed with no considerable impurity phase. The (200) and (020) peaks near $2\theta = 47°$ are characteristic of the existence of an orthorhombic phase as in the $YBa_2Cu_3O_{7-\delta}$ system [31].

For $0.0 \leq x \leq 0.15$, the orthorhombic structure with Pmmm symmetry, and for $0.2 \leq x \leq 0.5$, the tetragonal structure with P4/mmm symmetry has been used in the refinements. The total site occupation factors for O(1) and O(5) atoms (chain and antichain oxygens, respectively) were set to the iodometric titration measurement results for oxygen contents, which fluctuates between 6.96 to 7.06 for different $x$ values. For $x \geq 0.6$, the XRD patterns indicate that the 123 structure has not been formed, and their resistivities are a few orders of magnitude larger than for the $x < 0.6$ samples. Figure 2 shows the XRD pattern for $x = 1.00$. It is evident from the figure that the impurity peaks have appeared at about 25°, 30°, 31°, 36°, 45°, and 57°; the 123 phase peaks at about 79° and 87° have also disappeared, and the peaks at 53° and 69° have been deformed with respect to the 123 phase peaks.

Variation of lattice parameters with the amount of Pr doping ($x$) in $Gd(Ba_{2-x}Pr_x)Cu_3O_{7+\delta}$ are shown in Figure 3. The lattice parameter $a$ increases and $b$ decreases until for $x = 0.2$ the orthorhombic-tetragonal (O-T) phase transition occurs. This transition is due to the O(5) (0.5, 0.0, 0.0) occupation, which in turn is due to the appearance of $Pr^{3+}$ at $Ba^{2+}$ sites, requiring more negative charge. At $x = 0.2$, the coexistence of O(1) chain and O(5) antichain oxygen make the $a$ and $b$ directions equivalent; hence, the tetragonal phase forms. The total oxygen contents of samples are more than the optimum value in $R_{1-x}Pr_x$-123 systems [32], which is also the reason for the mentioned O-T transition. The O-T transition has also been reported in other $R(Ba_{2-x}R'_x)Cu_3O_{7+\delta}$ systems [15].

The final results of the Rietveld refinement are presented in Table 1. These include lattice parameters ($a$, $b$, and $c$), site occupation factors (N), isotropic displacements (B), relative position of atoms in $c$ direction (Z), $R$-factors of the Rietveld refinement: Pattern $R$-factor ($R_p$), weighted pattern $R$-factor ($R_{wp}$), Bragg $R$-factor ($R_B$), structure $R$-factor ($R_F$), and the quality of the fit parameter ($S$). The goodness parameter of refinement $S$ is close to 1, which is in support of the reliable results [29]. The interesting result is that for the special values of $0.05 \leq x \leq 0.30$, the Ba atom occupies the R site (Fig. 4); the $Ba_R$ mis-substitution has the highest value at $x = 0.2$. We will discuss this feature in Section 2. For more details of the Rietveld refinement process see reference [20].

With Pr substitution at Ba site, the perovskite substructures containing Pr become similar to the R containing perovskite sub-structures. So, $Pr_{Ba}$ makes its environment the same as Pr at rare earth site ($Pr_R$)

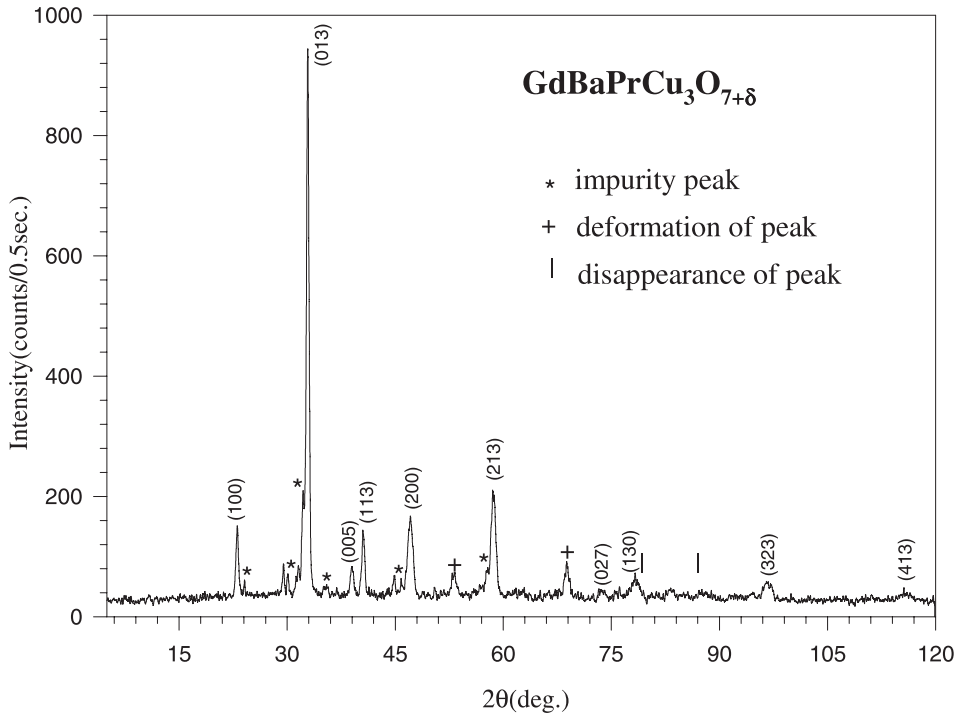


**Fig. 2.** The observed XRD pattern of $x = 1.00$ sample. The $(*)$ is impurity peak, the $(|)$ is the vanished 123 phase peak, and $(+)$ is deformed peaks in respect to 123 peaks.

**Table 1.** The Rietveld refinement results with variable N(O(4)) and N(O(1))=N(O(5)). For notation details see the text.

| $x$ | 0.00 | 0.05 | 0.10 | 0.15 | 0.20 | 0.25 | 0.30 | 0.40 | 0.50 |
|---|---|---|---|---|---|---|---|---|---|
| $a$(Å) | 3.847 | 3.847 | 3.855 | 3.860 | 3.870 | 3.868 | 3.869 | 3.868 | 3.865 |
| $b$(Å) | 3.890 | 3.889 | 3.888 | 3.881 | - | - | - | - | - |
| $c$(Å) | 11.696 | 11.692 | 11.667 | 11.660 | 11.645 | 11.633 | 11.607 | 11.579 | 11.564 |
| Gd N | 0.851 | 0.837 | 0.858 | 0.891 | 0.903 | 0.903 | 1.004 | 0.906 | 0.898 |
| B(Å) | 1.151 | 0.403 | 1.214 | 0.590 | 1.195 | 1.039 | 0.714 | 0.027 | 0.226 |
| Ba N | 0.999 | 0.982 | 0.977 | 0.937 | 0.973 | 0.901 | 0.811 | 0.805 | 0.746 |
| B(Å) | 3.241 | 3.668 | 2.030 | 0.380 | 1.356 | 1.201 | 0.875 | 0.188 | 0.387 |
| Z | 0.1811 | 0.1808 | 0.1813 | 0.1830 | 0.1813 | 0.1819 | 0.1843 | 0.1817 | 0.1809 |
| $Ba_RN$ | - | - | - | 0.038 | 0.045 | 0.025 | 0.004 | 0.030 | 0.019 |
| Pr N | - | 0.026 | 0.051 | 0.076 | 0.093 | 0.123 | 0.149 | 0.176 | 0.237 |
| B(Å) | - | 2.966 | 2.328 | 0.678 | 1.177 | 1.022 | 0.1818 | 0.010 | 0.209 |
| Cu(2) B(Å) | 2.954 | 2.858 | 2.292 | 0.970 | 1.243 | 1.373 | 1.341 | 0.642 | 1.116 |
| Z | 0.3508 | 0.3515 | 0.3509 | 0.3517 | 0.3504 | 0.3503 | 0.3533 | 0.3501 | 0.3493 |
| O(1) N | 0.539 | 0.517 | 0.582 | 0.685 | 0.704 | 0.665 | 1.0 | 1.0 | 0.988 |
| O(2) Z | 0.3886 | 0.3815 | 0.379 | 0.367 | 0.375 | 0.374 | 0.367 | 0.363 | 0.3701 |
| O(3) Z | 0.3707 | 0.3765 | 0.380 | 0.371 | - | - | - | - | - |
| O(4) Z | 0.1524 | 0.1531 | 0.1570 | 0.157 | 0.1570 | 0.1570 | 0.1570 | 0.1596 | 0.1581 |
| O(4) N | 0.951 | 0.983 | 0.928 | 0.815 | 0.801 | 0.865 | 0.423 | 0.389 | 0.4923 |
| $R_p$(%) | 10.732 | 10.444 | 12.478 | 11.333 | 13.393 | 12.853 | 12.299 | 10.969 | 12.278 |
| $R_{wp}$(%) | 13.809 | 13.410 | 16.163 | 14.631 | 17.399 | 16.679 | 15.538 | 14.115 | 15.709 |
| $R_B$(%) | 8.19 | 6.82 | 7.38 | 6.79 | 7.47 | 6.97 | 5.99 | 6.06 | 6.60 |
| $R_F$(%) | 7.55 | 6.79 | 8.61 | 7.39 | 9.57 | 8.98 | 6.77 | 6.70 | 8.28 |
| $S$ | 1.155 | 1.137 | 1.112 | 1.118 | 1.130 | 1.123 | 1.118 | 1.130 | 1.139 |

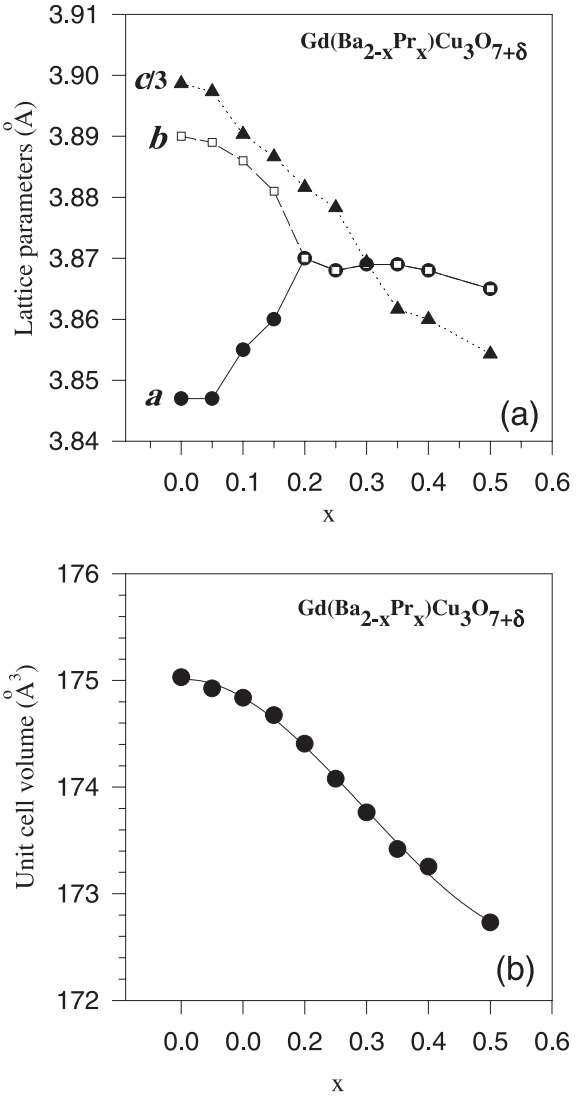


**Fig. 3.** (a): The lattice parameters, and (b): Unit cell volume vs. amounts of Pr doping ($x$). The lines are guides to the eye.

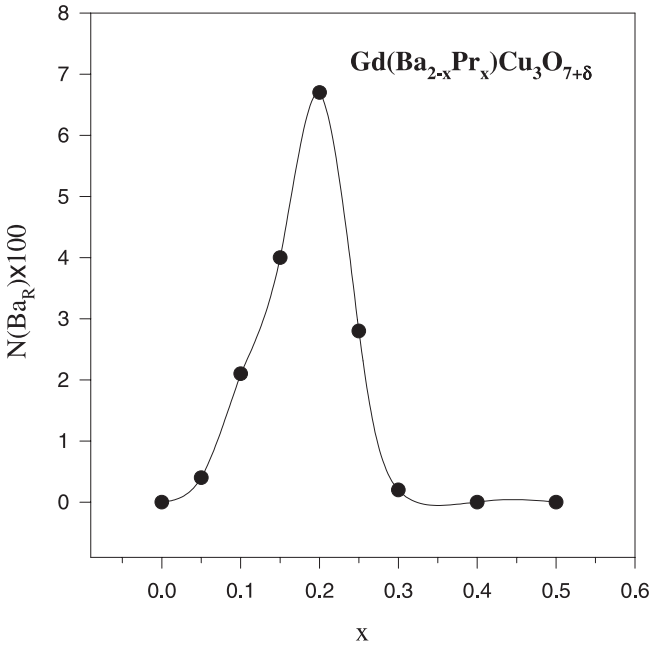


**Fig. 4.** Site occupation factor percent of Ba atoms at R site vs. different amounts of Pr doping ($x$). The line through the points is a guide to the eye.

but, due to the solubility limit, this process can only be followed to a certain extent. The amount of oxygen in $Eu(Ba_{2+x}Pr_x)Cu_3O_{7-\delta}$ for $0.0 \leq x \leq 0.7$ is less than 6.964 [33,34], in $Er(Ba_{2-x}La_x)Cu_3O_{7-\delta}$ for $0.0 \leq x \leq 0.3$ is at most 7 [32], and in $Sm(Ba_{2-x}Pr_x)Cu_3O_{7-\delta}$ for $0.0 \leq x \leq 0.2$, is from 6.96 to 7.04, respectively [35]. This small amount of oxygen, in spite of appearance of $R^{3+}$ at $Ba^{2+}$ site, supports our idea that with the increase of $x$ the O(4) atom migrates from its original position. This retains the coordination number close to 8 for Pr atoms at the Ba site, and the total oxygen content of the samples remains less than or about 7. Therefore, it seems that formation of the incomplete perovskite sublattices in the 123 structure is the principle behind the mis-substitution scenario.

In Zou's claimed superconducting Pr-123 samples [5], one possibility for the larger $c$ lattice parameter with respect to the typical 123 structures, have been proposed to be the presence of Ba atoms at Pr sites ($Ba_R$). Narozhnyi et al. [36,37], based on the effective magnetic moment of Pr atom, have concluded that in Zou's superconducting Pr-123 samples there should be some Ba atoms at Pr sites; $Ba^{2+}$ on R site dopes additional mobile holes and compensates the localization of holes by the Pr-O(2,3) hybridization. They have mentioned that the substitution of Ba for Pr could be a natural explanation not only for the superconductivity in Pr-123, but also for the elongation of the distances between the $CuO_2$ planes observed in reference [5]. It is noteworthy that Zou and Nishihara [37] have also confirmed that based on the effective magnetic moment of Pr in Pr-123, $Ba_R$ could be a possible explanation for the superconducting Pr-123. Therefore, if superconductivity occurs in the unit cells with $Ba_R$, the resistivity would decrease at a temperature, we call $T_m$. However, due to the large insulating parts of the sample, with Pr-substituted, the resistivity would not decrease to zero till the Josephson coupling energy between superconducting parts exceeds the thermal energy of the order of $k_BT$. Then, the superconducting transition occurs. In the electronic properties section, we will follow up on this scenario in detail.

In summary, the structural study of GdBaPr-123 samples show that the exact position of Pr and O(4) in the unit cell is crucial for understanding the role of Pr in suppression of superconductivity in the 123 structure of HTSC. This may also explain the claimed existence of superconductivity in Pr-123. The final test to check the legitimacy of the presented picture requires more investigations including experiments to directly detect the exact atomic positions in the compound.

## 2. Electronic properties

The resistivity of samples is presented in Figure 5. With the increase of $x$, the superconducting transition temperature decreases and the width of transition temperature ($\Delta T_c$) as well as the normal state resistivity increases, similar to $(Gd_{1-x}Pr_x)Ba_2Cu_3O_{7-\delta}$ system [38]. With the increase of number of insulating parts in the grain (i.e. Pr substituted unit cells), the homogeneity of grains decreases, which leads to larger $\Delta T_c$. In the samples with $x \leq 0.35$, the superconducting transition occurs, while for $x \geq 0.4$ there is no transition down to 10 K. So, the critical doping for SIT is $x_c^{\rm SIT} = 0.35$. The $x_c^{\rm SIT}$ in this compound is less than the one for $(Gd_{1-x}Pr_x)Ba_2Cu_3O_{7-\delta}$ compound, i.e. 0.45 [39]. This means that the suppression of superconductivity by Pr positioned at a Ba site is more effective than Pr at a R site. For the Pr at R site, we have an isovalent substitution of $R^{3+}$ by $Pr^{3+}$, while in the $Pr^{3+}$ at $Ba^{2+}$ site, an effect on carrier density is expected due to different valency of $Pr^{3+}$ and $Ba^{2+}$. Another plausible explanation for this is that the Ba site is located between the $CuO_2$ superconducting plane and Cu-O charge reservoir chains [40], which both have proved to be essential for superconductivity of 123 systems. Hence, the existence of Pr atoms between these two correlated parts would be more destructive than when Pr is positioned at the R site, which is between the two independent $CuO_2$ planes.

The $\rho_{100}$ changes linearly in the $0.00 \leq x \leq 0.50$ range, but at $x > 0.35$ the slope of the line changes (inset to Fig. 5). This means that the normal state resistivity behaves differently depending on the samples' status, i.e. superconducting or non-superconducting. This is an important exhibition showing that the normal state of HTSC has inherent information on the superconducting state of the system [41].

The resistivity of $0.15 \leq x \leq 0.30$ samples, has a striking hump feature on the curves above $T_c$ at $T_m \sim 80$–$90$ K. Based on the Rietveld refinement of XRD patterns and bond valence sum calculations we have found that the Ba atom substitution at the rare earth site could lead to superconductivity in some parts of the grains at $T_m \sim 80$–$90$ K, which appears as a hump on the $\rho(T)$ curve. The complete discussion of this effect has been presented in reference [20].

Recently, the resistivity of $(Pr_{1-x}Ba_x)Ba_2Cu_3O_{7-\delta}$ [42] have revealed that the resistivity increases with the increase of Ba doping at Pr site to about $x = 0.05$, and then deceases. But, for $x > 0.3$, due to the solubility limit and the non-123 phase formation, the resistivity increases drastically. The authors have proposed that Ba doping at Pr sites could revive the superconductivity in Pr-123 if by some particular sample preparation technique the solubility limit could be pushed to higher $x$ values.

The normal state resistivities for $x < 0.2$ samples are metal-like ($d\rho/dT > 0$), but for $x > 0.2$ are insulating-like ($d\rho/dT < 0$). So, the critical doping for MIT is $x_c^{\rm MIT} = 0.2$ while, the critical doping value for SIT is $x_c^{\rm SIT} = 0.35$. It is important to distinguish between the critical $x$ for SIT and MIT. It is worth noting that MIT does not necessarily occur at the concentration that superconductivity disappears, as we have worked out in detail and listed for different compounds [41]. We are interested to find the most appropriate conduction mechanism(s) in the whole range of normal states. So, the temperature domain of $T_c < T < 300$ K for the superconducting samples, and 10 K $< T <$ 300 K for the non-superconducting samples have been considered.

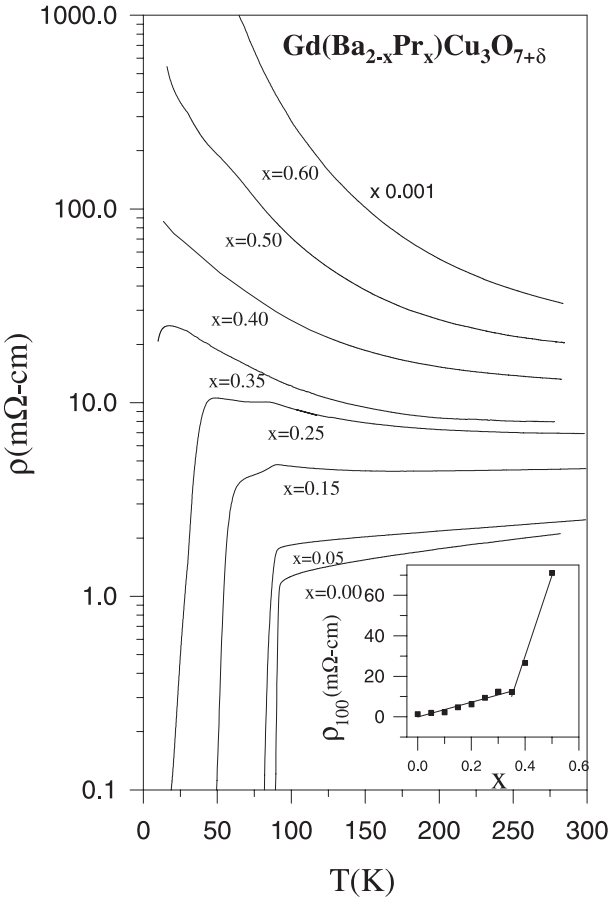


**Fig. 5.** Resistivity curve for $Gd(Ba_{2-x}Pr_x)Cu_3O_{7+\delta}$ samples in the range 10 K $< T <$ 300 K for $0.0 \leq x \leq 0.5$. The inset shows the resistivity at $T = 100$ K vs. $x$.

The best known examples for hopping conduction are due to Mott and Davis, and Shklovskii and Efros [43]. For these two cases, the temperature dependence of resistivity is $\rho(T) = \rho_0(T/T_0)^{2p}\exp(T_0/T)^p$, where $T_0$ is a characteristic temperature, which will be discussed later, and $p = (n+1)/(n+D+1)$. Here, $D$ is the dimensionality of the hopping process, and n describes the energy dependence of DOS in the vicinity of Fermi energy $N(E_F)$, which behaves like $N(E_F) \sim |E - E_F|^n$.

To test the VRH and CG regime, we have fitted 2D-VRH, 3D-VRH, and CG regimes separately for all the samples with $0.0 \leq x \leq 1.0$ (i.e., fixed-p method). However, it would be more appropriate to leave the exponent value $p$ as a variable, and obtain the valid regime automatically (i.e., the variable-p method). These results are presented in Figure 6. For almost all the samples, the value of p tends to 1/3 with a reasonable quality fit, which corresponds to the 2D-VRH. The 2D behavior is the HTSC's

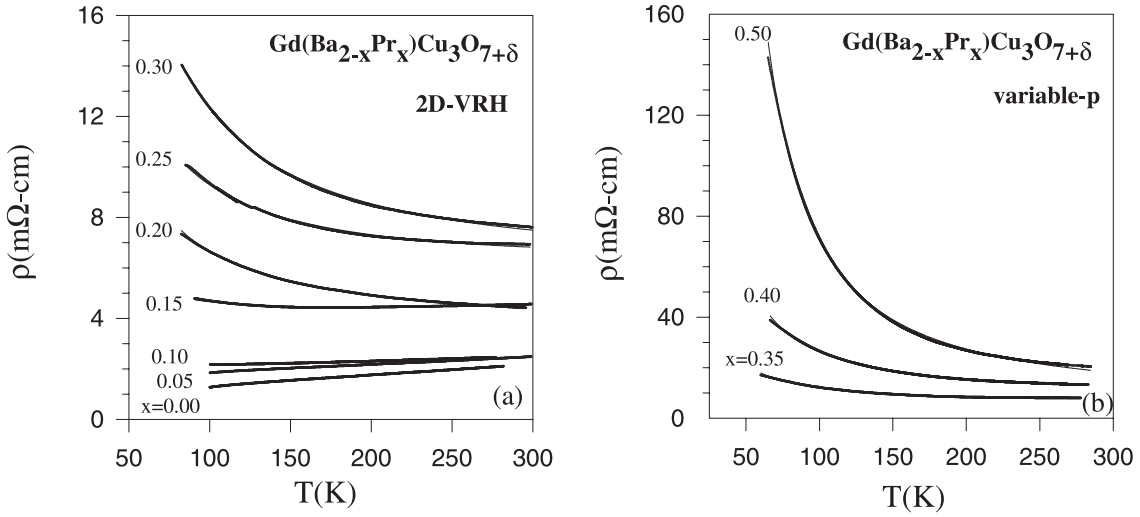


**Fig. 6.** (a) The 2D-VRH fit for $0.00 \leq x \leq 0.30$ of Pr doping ($x$). The dots appearing as a thick line are the experimental data, and the thin lines are the 2D-VRH regime predictions. (b) Hopping conduction fit with the variable-p method for $0.35 \leq x \leq 0.50$. The dots appearing as a thick line are the experimental data and the thin lines are the hopping conduction predictions.

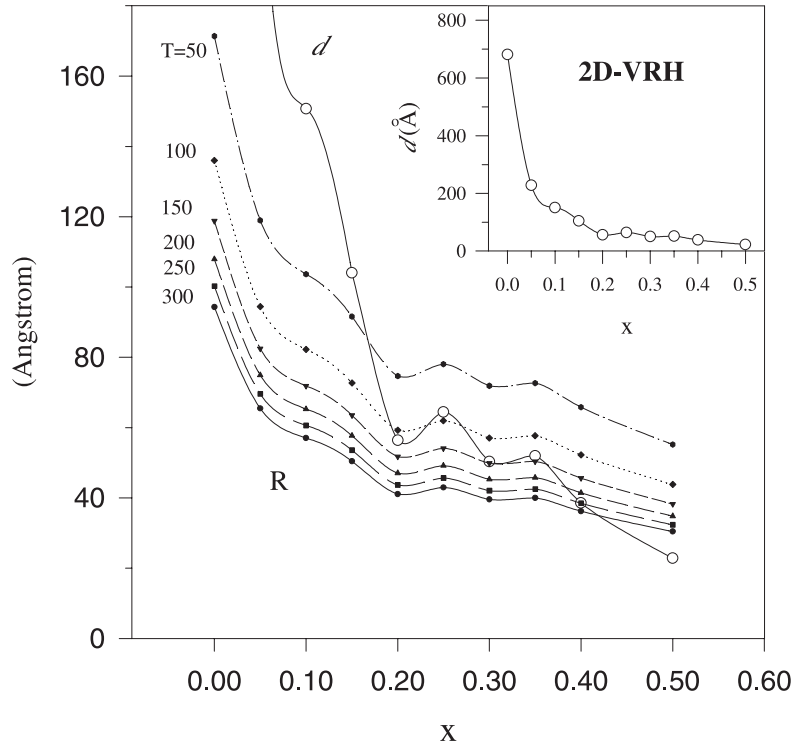


**Fig. 7.** The localization length ($d$) and hopping range ($R$) versus different amounts of Pr doping ($x$), calculated from the results of the variable-p method. The inset shows $d$ versus $x$ in the full range. The lines are guides to the eye.

well known characteristic, which has been established for many years [44], and we will elaborate more on that later.

The localization length and hopping range [41] for different amounts of Pr doping are shown in Figure 7. The length of the localized wave functions is highest for Gd-123 ($x = 0.0$). This means that due to the very large $d$ with respect to the distance of the neighboring atoms, the overlap of the carriers' wave functions is enough for the conduction to occur easily. Further, by Pr doping, the $d$ decreases. With the increase of $x$, due to the decrease of localization length, the hopping range decreases too. This means that Pr doping localizes the carriers in the normal state. When the localization length is very large, the extended carriers could facilitate the conduction process easily. Therefore, for small $x$, the hopping range is less than the localization length. As we know, for VRH mechanism, R should be larger than $d$. So, at low temperatures e.g. 50 K, and for $x \geq 0.20$, the 2D-VRH probably occurs in the $CuO_2$ planes. With increasing temperature, due to thermal fluctuations, hopping range decreases and the

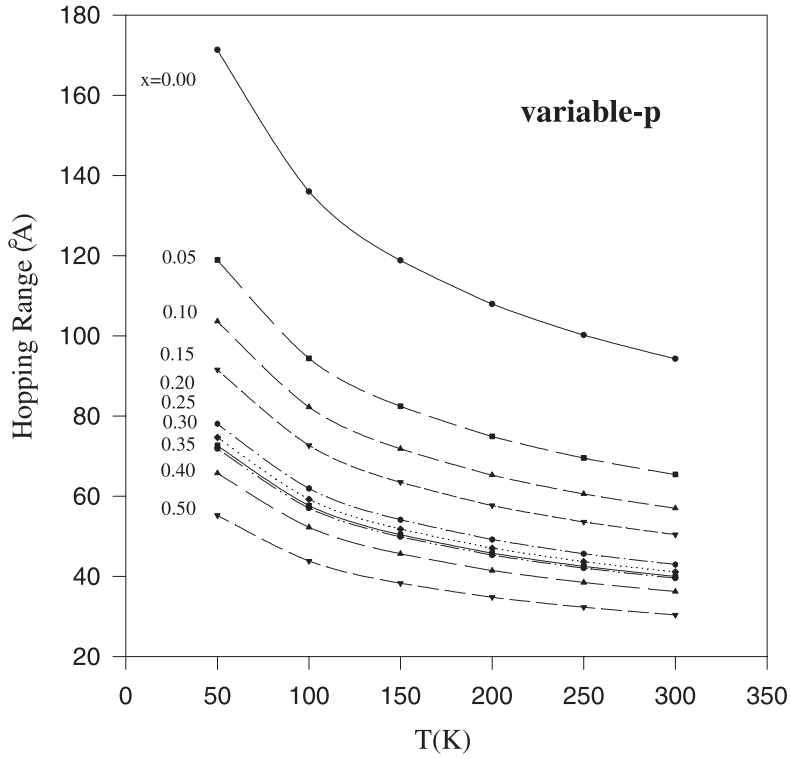


**Fig. 8.** The hopping range ($R$) versus temperature for different amounts of Pr doping ($x$), calculated from the results of variable-p method. The lines are guides to the eye.

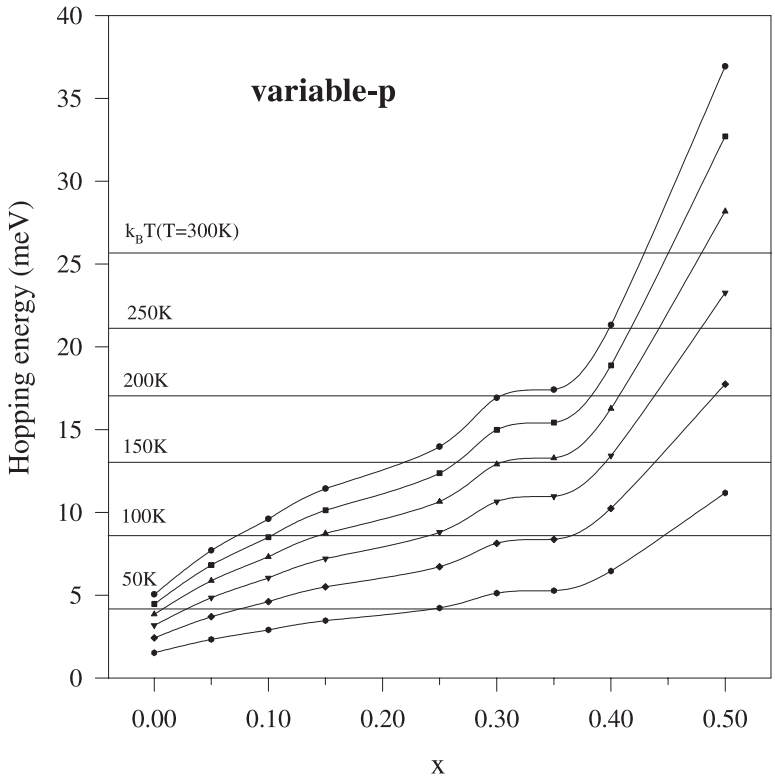


**Fig. 9.** The hopping energy ($W$) versus different amounts of Pr doping ($x$) for different temperatures, calculated from the results of variable-p method. The lines are guides to the eye.

threshold of $x$ ($x_t$), above which hopping occurs, changes; with the increase of temperature, $x_t$ increases.

The values of $R$ versus temperature are presented in Figure 8. With the decrease of temperature, the thermal fluctuations decreases and hopping occurs also for larger distances. This results in the increase of $R$, which agrees with the values of hopping range versus temperature in perovskites [45]. Our results are also consistent with the hopping range in Pr-123, which is 960 Å at 2 K [46].

Figure 9 shows the hopping energy versus $x$ for different temperatures. With the increase of Pr doping, due to the destructive effect of Pr on conduction, the required energy of carriers for executing the hopping conduction increases. For performing VRH, the hopping energy should

be larger than $k_BT$. For small temperatures, e.g. 50 K, due to small thermal fluctuations, a small amount of hopping energy is enough to allow hopping conduction. So, for $x \geq 0.20$, the VRH is a dominant mechanism of conduction in the normal state at $T = 50$ K. It is worth noting that with the increase of temperature, $x_t$ increases, which is exactly consistent with the extracted $x_t$ from the hopping range curves. With the increase of temperature, the hopping energy increases due to thermal fluctuations, which is destructive for hopping conduction. This result is also consistent with the changes of hopping energy versus temperature in perovskites [45].

In the metallic samples, the deviation of resistivity from linear behavior occurs at temperature $T_s$ at which pseudogap (or spin gap) opens. With the increase of Pr doping ($x$), the superconducting transition temperature, $T_c$ decreases as well as increasing the value of normal state resistivity. The slope of normal state resistivity vs. temperature systematically decreases with the increase of $x$. The $x$ dependence of $T_s$ for GdBaPr-123 and GdPr-123 compounds is presented in Figure 10. The GdPr-123 data have been extracted from our recent report [16]. In both systems with the increase of Pr doping, $T_s$ increases, but the change of $T_s$ in GdPr-123 is closer to a linear behavior than in the GdBaPr-123 compound. This is in agreement with other $R_{1-x}Pr_x$-123 compounds [47]. In GdBaPr-123 system, $T_s$ grows exponentially with $x$, and for a fixed amount of Pr doping, its $T_s$ is larger than the corresponding value for GdPr-123. This shows that the effect of Pr at Ba is stronger in changing the linear temperature dependence of resistivity and opening the pseudogap in comparison with the effect of Pr at R site.

Based on the above results, it is noteworthy that the real position of Pr in the constructed structure is important not only for superconducting properties [20], but also for the normal state behaviors [41,48]. Therefore, undesired substitution of Pr at Ba sites (mis-substitution) in $PrBa_2Cu_3O_{7-\delta}$ compound during the preparation process could have destructive effects on exhibition of superconductivity.

Figure 11 displays the $T_s$ vs. $T_c$ curves for GdBaPr-123, GdPr-123, and the oxygen deficient $GdBa_2Cu_3O_{7-\delta}$ samples. This plot shows that lower carrier density corresponds to higher pseudogap temperature. For a fixed $T_c$ of Gd-123-based sample, the $T_s$ depended on the oxygen content of the sample, and also on the position of Pr in the substituted structure. For a fixed $T_s$, due to the decrease of hole carrier number with decreasing $T_c$, the GdBaPr-123 system has the least amount of hole carrier in the $CuO_2$ superconducting planes, the GdPr-123 sample has more, and the largest amount of hole carriers corresponds to the oxygen-deficient Gd-123 sample [49]. This is further evidence that the destructive effect of Pr at Ba site is more than Pr at R site [50]. For the oxygen deficient $RBa_2Cu_3O_{7-\delta}$ samples, due to the similar $T_s$ vs. $T_c$ behavior for different rare earth ions, it has been concluded that the rare earth elements on the R sites and the distance between adjacent $CuO_2$ planes have no significant influence on the pseudogap temperature [45]. Based on our results,

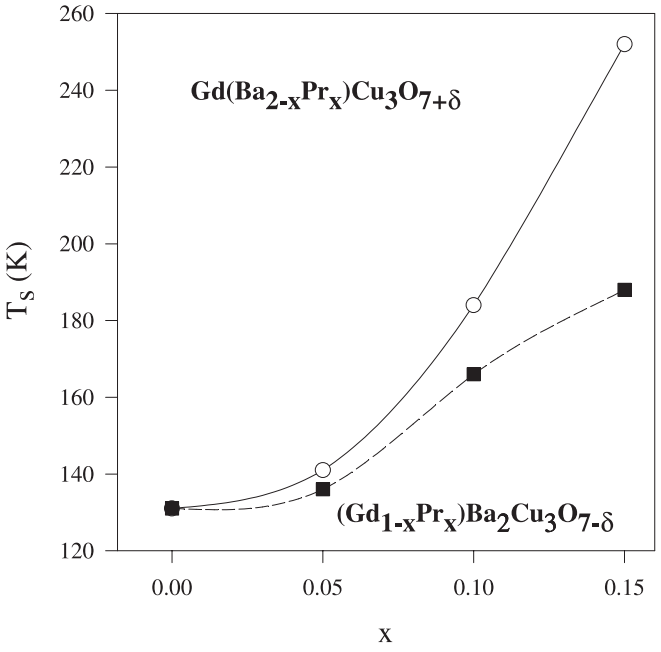


**Fig. 10.** Pseudogap temperature vs. different amounts of Pr doping ($x$) for $Gd(Ba_{2-x}Pr_x)Cu_3O_{7+\delta}$ and $(Gd_{1-x}Pr_x)Ba_2Cu_3O_{7-\delta}$. The lines are guides to the eye.

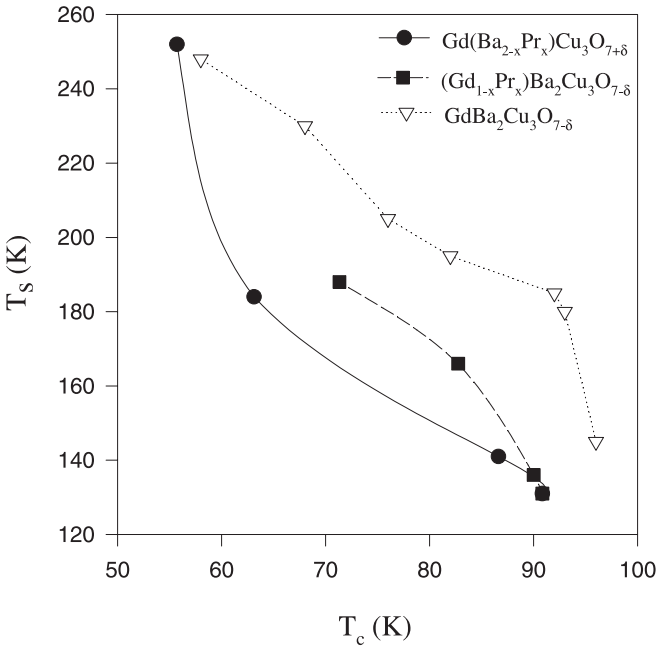


**Fig. 11.** Pseudogap temperature $T_s$ vs. $T_c$ for $Gd(Ba_{2-x}Pr_x)Cu_3O_{7+\delta}$, $(Gd_{1-x}Pr_x)Ba_2Cu_3O_{7-\delta}$, and oxygen deficient $GdBa_2Cu_3O_{7-\delta}$ (after Ref. [51] data). The lines are guides to the eye.

it is interesting that for Pr-substituted 123 structure, $T_s$ depends not only on the Pr position in the structure, but also on the amount of oxygen content in the sample. So, the correlation of superconducting gap and the normal state pseudogap is evident from the $T_s$ vs. $T_c$ curves. This is also consistent with the $c$-axis oriented $NdBa_2Cu_3O_{7-\delta}$ thin films results [51].

There are also some similar characteristics of HTSC, two dimensional electron gas (2D-EG), and ultra-thin films of conventional superconductors as follows: 1) MIT under variation of carrier density, thickness of ultra-thin films, and applied magnetic field, 2) localization of carriers in normal state of HTSC and insulating phase of 2D-EG, 3) quantum unit of resistance at SIT in superconductors and MIT at 2D-EG systems, and 4) larger change of resistance from critical doping to insulating phase in comparison with change of resistance from critical doping to metallic state. For more details see reference [52]. Neither the HTSC mechanism, nor MIT in 2D systems have been fully understood, but the evidence of similarities presented suggests they may be attributed to a unique origin of completely 2D-character of HTSC, or the real 2D-character of HTSC. In addition, these similarities may confirm the superconducting characteristic of metallic phase in 2D-EG systems, which have also been proposed.

In summary, the appropriate conduction mechanism in the normal state is 2D-VRH. With the increase of Pr doping, hopping conduction decreases, and the localization length and hopping range decrease, while the hopping energy increases, consistent with $d$ and R variations. The localization of carriers in the normal state with Pr doping causes the suppression of superconductivity in Pr-doped systems. By comparing the $x_c^{\mathrm{SIT}}$, $T_s - x$, $T_s - T_c$, and phase diagrams of $Gd(Ba_{2-x}Pr_x)Cu_3O_{7+\delta}$ and $(Gd_{1-x}Pr_x)Ba_2Cu_3O_{7-\delta}$ compounds, we have concluded that the destructive effect of Pr substitution at Ba site is more pronounced than Pr at R site for superconductivity suppression in Gd-123 based HTSC.

## 3. Flux dynamics

The electronic properties of HTSC are affected by applying a magnetic field [53]. Therefore, in this section we will study the magnetoresistance properties of the samples. The magnetic field dependence of the resistivity for $x = 0.00$, 0.05, and 0.10 samples is shown in Figure 12 for the range of 0 to 20 kOe. A very small change of the normal state resistivity and a noticeable broadening of superconducting transition is observed in the resistivity curve with the application of magnetic field. With increasing the applied magnetic field, the $T_c^{\mathrm{onset}}$ remains almost constant, while $T_c(\rho = 0)$ decreases considerably. The change of resistivity in the mixed state region, due to the thermally activated flux creep near $T_c^{\mathrm{onset}}$, is less sensitive to the magnetic field; the tail part near $T_c^{\mathrm{mid}}$, associated with the weak links between the grains [54], is more sensitive to the magnetic field. For the samples with $x \leq 0.25$, the distinction between the steep and tail parts seems less pronounced, as is clear from Figure 13. For $x < 0.15$, due to small amount of Pr doping, there are intragrain regions, where the magnetic field has no influence on. So, there are two distinct –steep and dissipative– parts corresponding respectively to the intergrain and intragrain regions. With doping larger amounts of Pr i.e. $x \geq 0.15$, there are enough Pr-doped unit cells, which play the role of weak links. Hence, for these values of Pr doping, the magnetic field influences the weak links, including the empty space and the Pr-doped unit cells in between the superconducting cells. From Figure 13, it is evident that for $x = 0.25$, application of magnetic field higher than 5 kOe will cause a superconductor-insulator transition (SIT). This is an important effect, which is similar to the 2D-EG systems [52]

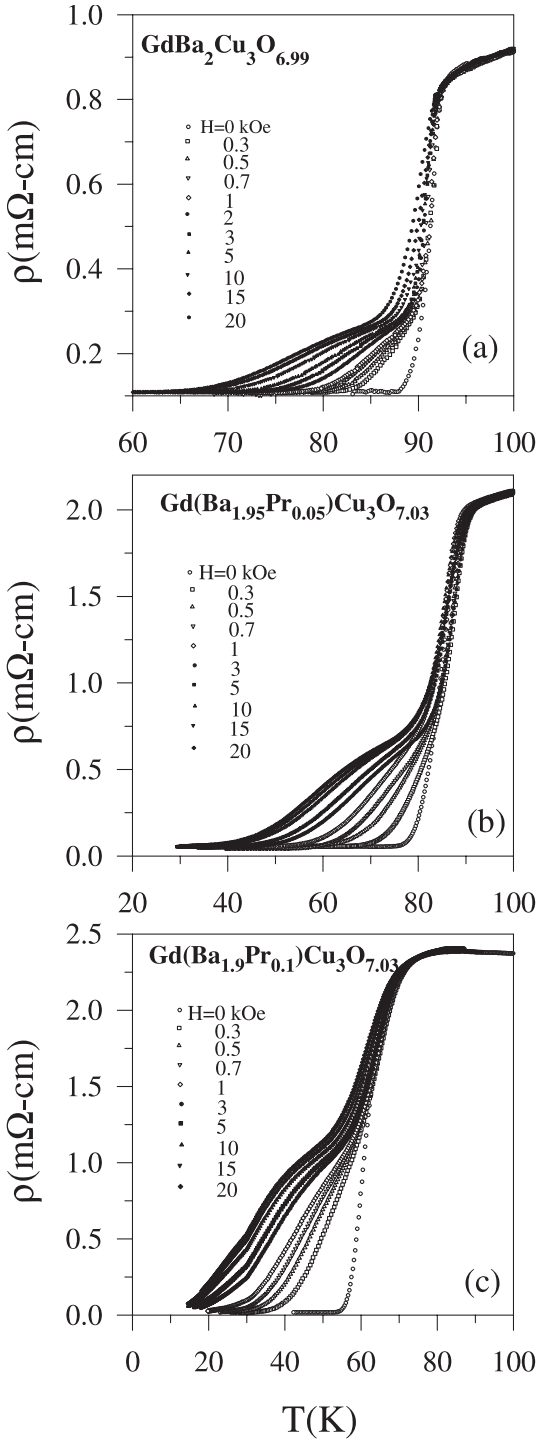


**Fig. 12.** Resistivity vs. temperature for (a): $x = 0.00$, (b): $x = 0.05$, and (c): $x = 0.10$ samples under different applied magnetic fields.

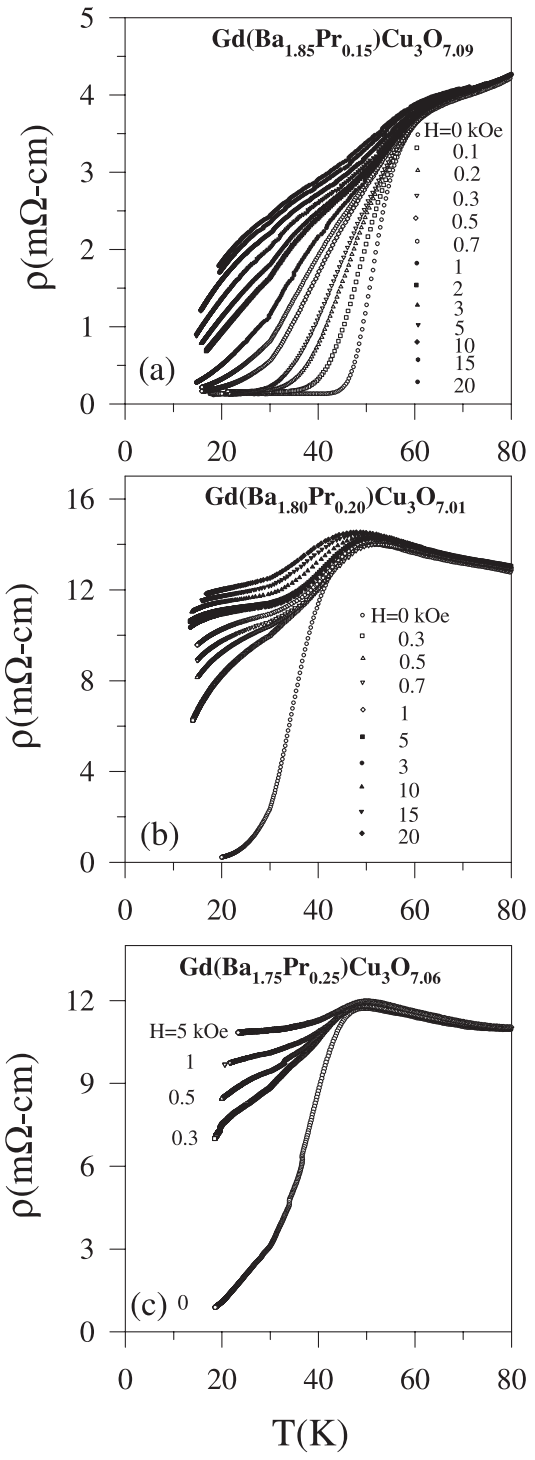


**Fig. 13.** Resistivity vs. temperature for (a): $x = 0.15$, (b): $x = 0.20$, and (c): $x = 0.25$ samples under different applied magnetic fields.

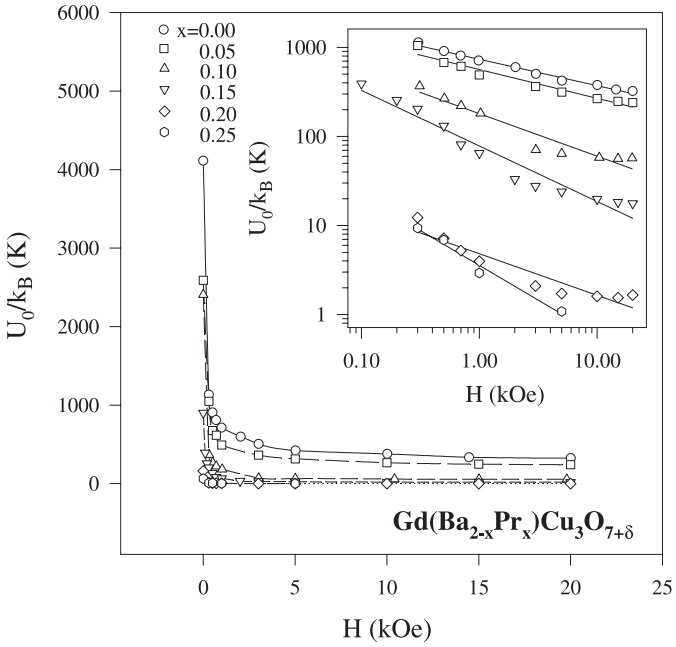


**Fig. 14.** Pinning energy vs. applied magnetic field for different amounts of Pr doping ($x$). The inset is its log-log representation.

as explained before. It is interesting that the critical value of Pr doping for the corresponding distinction is close to the critical value of Pr doping for metal-insulator transition (i.e., $x_c^{\mathrm{MIT}} = 0.20$).

The resistivity transition in the polycrystalline HTSC in the applied magnetic field has been found to obey the Arrhenius relation $\rho(H,T) = \rho_0 \exp(-U_0(H,T)/k_BT)$ [55,56]. Here, $U_0$ is the pinning energy that depends on temperature and magnetic field. The functional dependence of $\rho(H,T)$ is expected to give information about the mechanism of dissipation. The derived flux pinning energy, $U_0$ from the above fitting at different magnetic fields for different amounts of Pr doping is presented in Figure 14. For each $x$, the flux pinning energy decreases with the increase of applied magnetic field. This is in agreement with the reports for epitaxial $YBa_2Cu_3O_{7-\delta}$ thin films [57], single crystal of $Bi_{2.2}Sr_2Ca_{0.8}Cu_2O_{8+\delta}$ [58], and polycrystalline GdPr-123 samples [59]. The deduced value of pinning energy is in good agreement with the corresponding values in GdPr-123 samples [60], and it is in the order of magnitude of other approaches for finding $U_0$, e.g. magnetic relaxation measurements in $Y_{1-x}Pr_x$-123 [61,62].

We have fitted a power law relation for $U_0$ vs. $H$ as $U_0 \sim H^{-\beta}$ for each sample, as is shown in the inset of Figure 14. The values of $\beta$ and the quality of fit for the power law dependence, $\chi^2$ for different amounts of Pr doping are presented in Table 2; the value of $\beta$ begins from 0.297 for $x = 0.00$ and increases to 0.782 for $x = 0.25$. An important point is that with the increase of $x$, as is evident from $\chi^2$, the power law relation becomes less valid. Our result is consistent with the Palstra et al. [55] result for the $Bi_2Sr_2CaCu_2O_{8-\delta}$ system, where $\beta$ depends on the orientation of magnetic field with respect to the basal plane and the range of magnetic field i.e., smaller or greater than 30 kOe.

On re-examining the log-log plot of $U_0$ vs. $H$ of Figure 15a for all samples, a break about $H = 1$ kOe is evident. Quantitatively, the values of $\beta$ and $\chi^2$ in different regions of $H$ are presented in Table 3. As is evident

**Table 2.** The $\beta$ factor and the quality of fit $\chi^2$ for different amounts of Pr doping ($x$).

| $x$ | $\beta$ | $\chi^2$ |
|---|---|---|
| 0.00 | 0.297 | 0.987 |
| 0.05 | 0.323 | 0.952 |
| 0.10 | 0.477 | 0.924 |
| 0.15 | 0.623 | 0.947 |
| 0.20 | 0.467 | 0.895 |
| 0.25 | 0.782 | 0.980 |

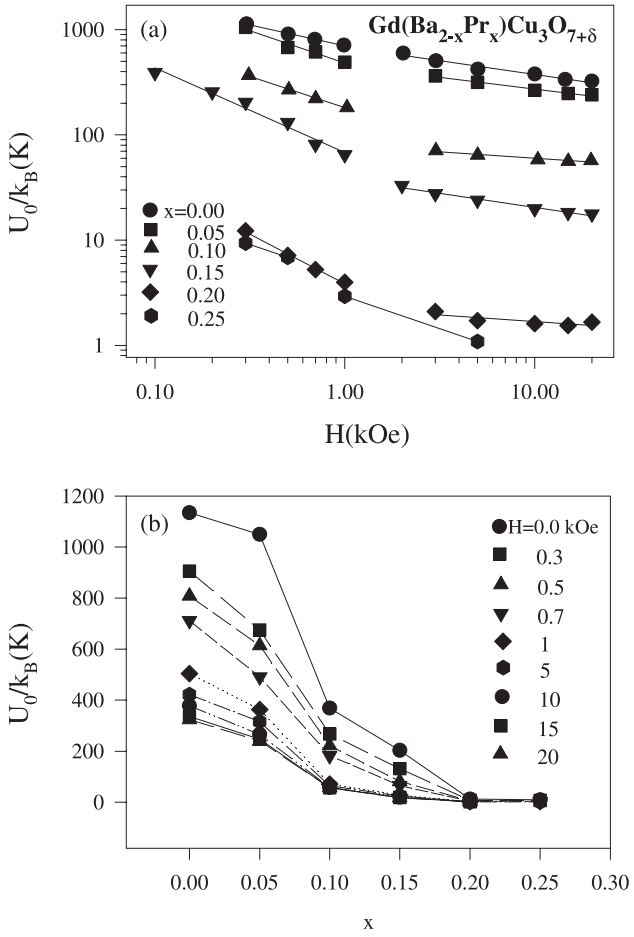


**Fig. 15.** (a): Pinning energy vs. applied magnetic field for different amounts of Pr doping ($x$). The linear behavior of pinning energy is separated into two parts: Less than and greater than 1 kOe. (b): Pinning energy vs. Pr doping ($x$) for different applied magnetic fields.

from $\chi^2$, the $U \sim H^{-\beta}$ fit is more suitable for $H < 1$ kOe (completely) than for $H > 1$ kOe (almost). In epitaxial $c$-oriented Gd-123 thin films, with increasing the applied magnetic field, a crossover of the $\beta$ value from 0.5 to 1.0 at about 10 kOe for $H||ab$ and 8 kOe for $H||c$ has been observed [63]. We think that the origin of the two-linear-part in $\ln U_0$ vs. $\ln H$ curve is that the linear part in $\ln \rho - 1/T$ plots become less valid with the increase of $x$. In other words, with the increase of Pr doping, the temperature dependence of $U_0$ becomes stronger. This shows

**Table 3.** The $\beta$ factor and $\chi^2$ for different amounts of Pr doping ($x$) for two separated ranges of magnetic field: Smaller and larger than 1 kOe.

| $x$ | $H < 1$ kOe | | $H > 1$ kOe | |
|---|---|---|---|---|
| | $\beta$ | $\chi^2$ | $\beta$ | $\chi^2$ |
| 0.00 | 0.394 | 0.996 | 0.261 | 0.971 |
| 0.05 | 0.611 | 0.966 | 0.223 | 0.985 |
| 0.10 | 0.594 | 0.996 | 0.121 | 0.923 |
| 0.15 | 0.804 | 0.978 | 0.269 | 0.980 |
| 0.20 | 0.942 | 0.995 | 0.125 | 0.683 |
| 0.25 | 0.609 | 1 | 0.618 | 1 |

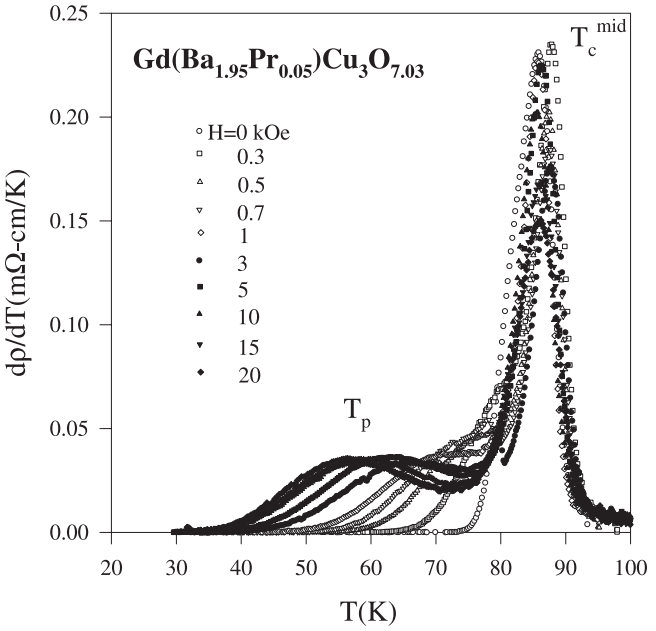


**Fig. 16.** Temperature derivative of magnetoresistance curves vs. temperature for $x = 0.05$ sample. The smaller peak at $T_p$ corresponds to the intergranular flux creep.

that the more advanced models such as thermally activated Ambegaokar and Halperin phase slip model might be more suitable for this system [53].

The Pr doping dependence of $U_0$ is shown in Figure 15b. With the increase of $x$, the pinning energy decreases. As we concluded earlier, the Pr substitution behaves like weak links. With the increase of weak links, the vortices are able to creep more easily, and the pinning energy decreases. Our result is consistent with the Pr-doped GdPr-123 [64], Ca-doped GdPr-123 [65], and YPr-123 system [66].

The $\mathrm{d}\rho/\mathrm{d}T$ vs. $T$ curve at $H = 0$ has only one peak at $T_c^{\mathrm{mid}}$, as is shown in Figure 16. However, upon the application of magnetic field, another peak emerges, which is related to the dissipative tail part of resistivity. In the range of applied magnetic field in our study, $0 < H \leq 20$ kOe, the changes in $T_c^{\mathrm{mid}}$ is small, as is evident from Figure 12. This is due to the large intragrain $H_{c2}$. However, the

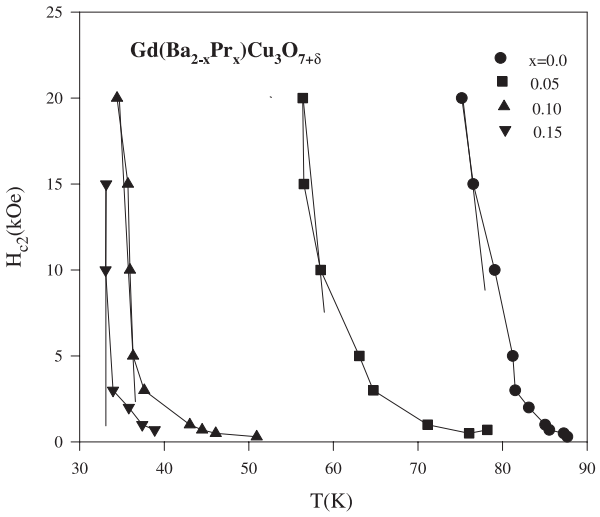


**Fig. 17.** Intergranular upper critical magnetic field vs. temperature for different amounts of Pr doping ($x$). The tangent lines are used to find $H_{c2}(0)$ (see the text).

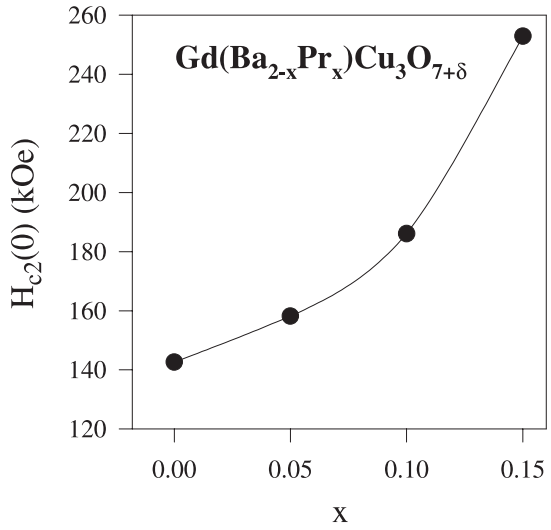


**Fig. 18.** Upper critical magnetic field at zero temperature limit vs. Pr doping ($x$).

range of magnetic field used is enough to change the intergrain coupling. So, the maximum of the smaller peak in $\mathrm{d}\rho/\mathrm{d}T(T_p)$ shifts with $H$. $T_p$ is defined as the critical temperature at 50% of intergrain weak links resistivity. We will use $T_p$ to find the intergranular upper critical field $H_{c2}$. It is reported that the $H_{c2}(T)$ curve determined from resistivity using the 50% criterion gives the best agreement with those determined from I-V curves [67].

Figure 17 shows the intergranular $H_{c2}$ vs. $T$ for $0.00 \leq x \leq 0.15$. $T_p$ for $x = 0.20$ and 0.25 samples under applied magnetic field is less than 10 K, which was not accessible for us. These curves show the critical values of magnetic field to annihilate the intergranular weak links. These curves are similar to the $H||ab$ plane and $H \perp J$ curves for Gd-123 thin films [63]. Since in the $H||c$ and $H \perp J$ case, $H_{c2}$ vs. $T$ curve is linear, it is concluded that the GdBaPr-123 intergrain coupling resembles a 2D-system behavior.

Due to the very large upper critical field at $T = 0$ limit in HTSC, the slope of $H_{c2}$ vs. $T$ curve at the highest field and its extrapolation to zero temperature have been used to find $H_{c2}(0)$ [68]. We use the relation $H_{c2}(0) = 0.69[dH_{c2}(T)/dT]T'$, where the slope is chosen as explained above, and $T'$ is the intersection of the tangent with the temperature axis [69]. Using this method, the deduced $H_{c2}(0)$ for different $x$ is presented in Figure 18; $H_{c2}(0)$ increases rapidly with $x$. Although Pr doping is unsuitable for $T_c$, its effect on pinning the vortices it increases the upper critical field. This characteristic could be useful in practical application of HTSCs.

Another approach to the problem of flux dynamics in a magnetic field leading to induced dissipation behavior of the HTSC- has been achieved by applying the Ambegaokar and Halperin (AH) phase slip model [54] to a medium of Josephson weak links. Within this theory, when $k_BT$ becomes comparable with the Josephson coupling energy, the resistance $\rho(T)$ in the limit of low current, $I \ll I_c(T)$, is given by $\rho(T) = \rho_n[I_0(\gamma/2)]^{-2}$, where, $I_0$ is the modified Bessel function, $\rho_n$ is the average normal state resistivity of the junction, and $\gamma$ is the normalized barrier height for thermally activated phase slip, defined as $\gamma = U_0/k_BT = A(1-t)^q/H$ [54]. Here, $U_0$ is the activation energy, $t \equiv T/T_c$ is the reduced temperature, $H$ is the applied magnetic field, and A is a constant. In the fitting process, we use $\rho_n$, $C(H) \equiv A/H$, $T_c$, and $q$ as free parameters. A typical AH fit to the resistivity under magnetic field is shown in Figure 19 for $GdBa_2Cu_3O_{6.99}$ compound. For each curve, the four free parameters: $\rho_n$, $C(H)$, $T_c$, and $q$ have been determined from the fit. In order to avoid the ambiguity of the double transition during the fitting process for $x < 0.15$, the higher-temperature

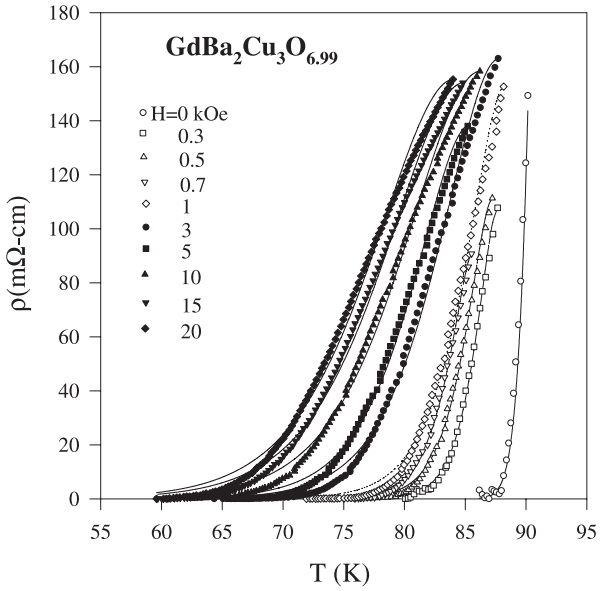


**Fig. 19.** AH phase slip fit (lines) for resistivity vs. temperature data (symbols) of $GdBa_2Cu_3O_{6.99}$ sample under different applied magnetic fields.

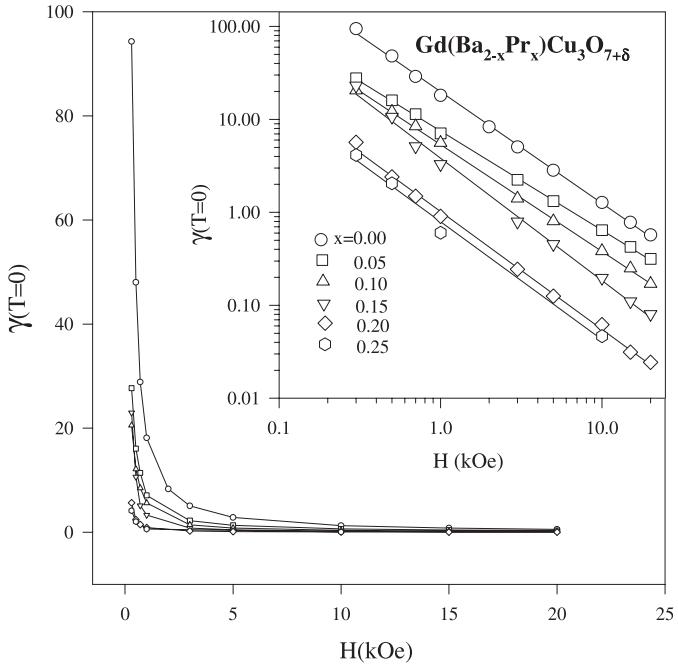


**Fig. 20.** The parameter $\gamma$ at zero temperature vs. $H$ of GdBaPr-123 samples for different amounts of Pr doping ($x$). The lines are guides to the eye. Inset shows the $\ln\gamma$-$\ln H$ fit.

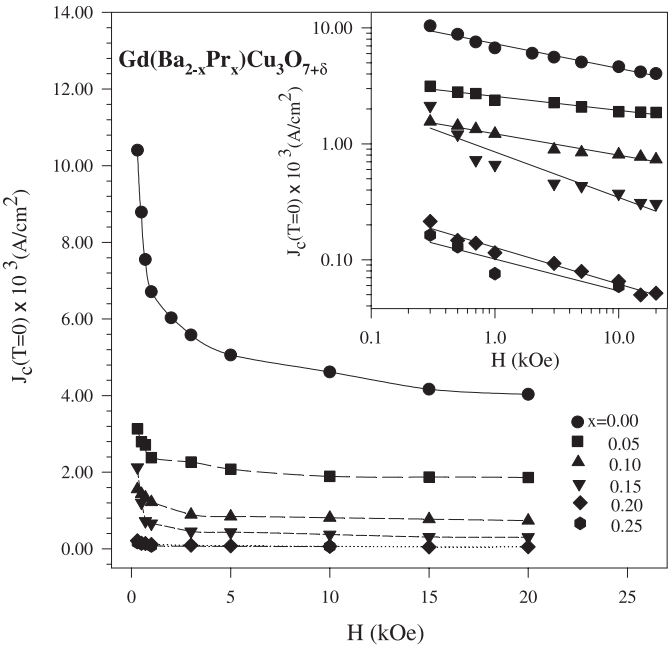


**Fig. 21.** Critical current density at zero temperature vs. $H$ of GdBaPr-123 samples for different amounts of Pr doping ($x$). The lines are guides to the eye. Inset shows the $\ln J_c - \ln H$ fit.

**Table 4.** The $\alpha$ and $\beta$ factors and oxygen content $7+\delta$ for different amounts of Pr doping ($x$).

| $x$ | $\alpha$ | $\beta$ | $7+\delta$ |
|---|---|---|---|
| 0.00 | 0.20 | 1.20 | 6.99 |
| 0.05 | 0.07 | 1.07 | 7.03 |
| 0.10 | 0.15 | 1.15 | 7.03 |
| 0.15 | 0.32 | 1.32 | 7.09 |
| 0.20 | 0.27 | 1.27 | 7.01 |
| 0.25 | 0.27 | 1.27 | 7.06 |

transition, which corresponds to the transition of the superconducting grains was excluded in the fitting of resistivities. Since, for every sample, the value of $\rho_n$ at the onset part of the resistivity tails are field independent and could easily be measured for an individual compound, it was concluded that these parameters could be determined from the experimental data without using them as free fitting parameters.

Figure 20 shows the pinning energy related-$\gamma$ vs. $H$ curves for the GdBaPr-123 compound. The inset to the figure shows clearly that $\gamma(H)$ is quite linear in the log-log plot. The corresponding slope (i.e., power factor in $\gamma \sim H^{-\beta}$) is presented in Table 4 for different amounts of Pr doping. The average value of $\beta$ is about 1.2. With the increase of magnetic field, the coupling energy between the Josephson vortices decreases. For each magnetic field, with the increase of Pr doping, $\gamma$ also decreases. The power law dependence of $\gamma$ with $H$ has also been reported by others, and is reviewed in reference [53].

From the AH phase slip theory, the parameter $C(H)$ at temperatures close to $T_c$ is given by $C(H) = J_{cj}(0)\hbar a^2/ek_BT_c$ where, $J_{cj}(0)$ is the critical current density at zero temperature and $a$ is the average grain size [70]. Considering the typical grain size in our samples to be $\sim$1 $\mu$m by the SEM measurements, the estimated values of $J_{cj}(0)$ for the GdBaPr-123 samples are presented in Figure 21. Due to using the intergranular magnetoresistance (MR) data, this $J_{cj}(0)$ has a more intergranular characteristic. However, with the increase of magnetic field, the critical current in the grain boundaries decreases significantly as a power law dependence $J_{cj}(0) \sim H^{-n}$, with $n \sim 0.2$. The decrease of $J_{cj}(0)$ with Pr doping suggests that Pr ions act as weak links, as has also been concluded through a thermally activated flux creep model [53]. Decreasing of the critical current with increasing $H$ is in agreement with the reports on Y-123 [71] and Ca-doped GdPr-123 [72,73], which in turn is an indication of the sensitivity of superconducting grain junctions to the applied magnetic field in these compounds. Moreover, for Y123 film boundaries, a continuously decreasing $J_c$ was measured at fields up to 20 kOe (similar to our domain of applied $H$) and $T = 77$ K. The order of magnitude of $J_{cj}(77)$ [74] is the same as our results. So, the AH phase slip model predicts a valuable grain boundary critical current density, which is in agreement with experimental results. This could enhance the validity of the AH model.

In summary, flux dynamics in GdBaPr-123 samples shows that Pr doping decreases the pinning energy, and hence, decreases the $H_{c2}$ and $J_{cj}$. Also, the AH phase slip model is proved to be more suitable in comparison with the thermally activated flux creep model in explaining the magnetoresistivity effects in GdBaPr-123 system. In addition, the magnetoresistivity data has inherent information on the dimensionality of the conduction mechanism in HTSC.

## Conclusions

We have prepared and studied polycrystalline $Gd(Ba_{2-x}Pr_x)Cu_3O_{7+\delta}$ samples with no significant impurity phase. In addition to indirect evidence from the Rietveld refinement results, it has been concluded that the expected structure of $Pr_{Ba}$ in Gd-123 has been formed. Moreover, with the substitution of Pr at Ba sites, the basic perovskite sub-structure becomes identical to a Pr at rare earth site perovskite, and hence, Pr at Ba or R site suppresses the superconductivity by the same mechanism(s). The mis-substitution of Ba at Gd sites occurs in some of the samples, which could be the origin of a hump on $\rho(T)$ curve at $T_m \sim 80$–$90$ K.

There are two distinct transitions: The MIT at $x_c^{\mathrm{MIT}} = 0.20$ and the SIT at $x_c^{\mathrm{SIT}} = 0.35$ in GdBaPr-123 compound. It is concluded that the appropriate conduction regime in the normal state is 2D-VRH. The localization of the carriers in normal state with Pr doping causes the suppression of superconductivity in Pr-doped systems. By comparing the $x_c^{\mathrm{SIT}}$, $T_s - x$, and $T_s - T_c$, of GdBaPr-123 and GdPr-123 compounds, we have concluded that the destructive effect of Pr substitution at Ba site is more pronounced than Pr at R site for superconductivity in Gd-123 based HTSC. The $T_s - T_c$ curves portray a correlation of superconducting gap and the normal state pseudogap. It is also shown that Pr doping, not only reduces the carrier density, which induces the pseudogap, but it also simultaneously increases $T_s$ and suppresses the linearity behavior of resistivity vs. temperature in the normal state.

Based on our magnetoresistance measurements, it is concluded that the pinning energy decreases with the increase of Pr doping, and exponentially with applied magnetic field. Moreover, a universal $\beta$ in power law relation of the pinning energy $U_0$ vs. $H$ is not accessible, but there is a break in the linear behavior of $\log U_0 - \log H$ curve at 1 kOe.

In addition, the derived intergranular $H_{c2}$ vs. $T$ shows strong positive curvature and no evidence of saturation at low temperatures. $H_{c2}(0)$ increases and the intergranular superconducting coherence length decreases with Pr doping. In comparison with GdPr-123 system, it is concluded that although Pr at Ba or R site plays the role of weak links, the effect of Pr at Ba sites is more destructive on superconductivity than Pr at R site.

Based on the AH phase slip model, the power law dependence of the pining energy related-$\gamma$ to magnetic field and temperature has been obtained for different amounts of Pr doping. The dispersivity in the power factors of our results with that of other reports could be due to different angles of grain boundaries, inhomogeneous grain microstructures, different amount of oxygen contents in grains, and various domains of applied magnetic fields. The critical current density vs. $H$ is consistent with directly measured intergranular $J_c$ both in its behavior and order of magnitude.

Pr substitution both at Ba and R sites, in each magnetic field, decreases the pinning energy and critical current density. Moreover, the magnetic dependence of power factor of $\gamma$ (i.e., q) is increasing for small amounts of Pr doping, while for larger amount of Pr doping, it is decreasing. Since, in our MR curves, the intergranular properties are dominant, the effect of Pr doping appears as weak links. The successful interpretation of magnetoresistance by using the AH phase slip model in small and large ranges of magnetic fields, enhances the validity of this model in comparison with the thermally activated flux creep model. Our comparison of the AH model predictions with experimental results confirms the validity of this model in both weakly coupled and strongly interacting grains.

Valuable results have been extracted from the data on Pr substitution at Ba (which is investigated for the first time) and R sites in Gd-123 compound. This has led to an explanation for the insulating and superconducting behavior of Pr-123 samples. We have shown that studies of the Pr singularity lead to a better understanding of superconductivity mechanism(s) in HTSC.

The authors wish to thank H. Khosroabadi, V. Daadmehr, G. Zolfagharkhani, and H. Shakeripour for technical assistance and fruitful discussions, and M. Sedaghat. This work was supported in part by the Offices of Vice President for Research and Dean of Graduate Studies at Sharif University of Technology.

## References

1. Z. Yamani, M. Akhavan, Phys. Rev. B **56**, 7894 (1997)
2. L. Soderholm, K. Zhang, D.G. Hinks, M.A. Beno, J.D. Jorgensen, C.U. Segre, I.K. Schuller, Nature **328**, 604 (1987)
3. H. Shakeripour, M. Akhavan, Supercond. Sci. Technol. **14**, 213 (2001)
4. H.A. Blackstead, J.D. Dow, Phys. Rev. B **51**, 11830 (1995)
5. Z. Zou, J. Ye, K. Oka, Y. Nishihara, Phys. Rev. Lett. **80**, 1074 (1998)
6. M. Luszczek, W. Sadowski, T. Klimczuk, J. Olchowik, B. Susla, R. Czajka, Physica C **322**, 57 (1999)
7. F.M. Araujo-Moreira, P.N. Lisboa-Filho, S.M. Zanetti, E.R. Leite, W.A. Ortiz, Physica B **284-288**, 1033 (2000)
8. T. Usagawa, Y. Ishimaru, J. Wen, T. Utagawa, S. Koyama, Y. Enomoto, Appl. Phys. Lett. **72**, 1772 (1998)
9. M. Akhavan, Physica B **321**, 265 (2002)
10. M. Akhavan, Phys. Stat. Sol. (b) **241**, 1242 (2004)
11. J.J. Neumeier, T. Bjornholm, M.B. Maple, I.K. Schuller, Phys. Rev. Lett. **63**, 2516 (1989)
12. G.Y. Guo, W.M. Temmerman, Phys. Rev. B **41**, 6372 (1990)
13. R. Fehrenbacher, T.M. Rice, Phys. Rev. Lett. **70**, 3471 (1993)
14. H.A. Blackstead, D.B. Chrisey, J.D. Dow, J.S. Horwitz, A.E. Klunzinger, D.B. Pulling, Phys. Lett. A **207**, 109 (1995)
15. M.J. Kramer, K.W. Dennis, D. Falzgraf, R.W. McCallum, S.K. Malik, W.B. Yelon, Phys. Rev. B **56**, 5512 (1997)
16. M.R. Mohammadizadeh, H. Khosroabadi, M. Akhavan, Physica B **321**, 301 (2002)
17. I.D. Brown, D. Altermatt, Acta Cryst. B **41**, 244 (1985); I.D. Brown, J. Solid State Chem. **82**, 122 (1989)

18. M. Imada, A. Fujimori, Y. Tokura, Rev. Mod. Phys. **70**, 1039 (1998)
19. S. Kleefisch, B. Welter, A. Marx, L. Alff, R. Gross, M. Naito, Phys. Rev. B **63**, 100507 (2001)
20. M.R. Mohammadizadeh, M. Akhavan, Phys. Rev. B **68**, 104516 (2003)
21. C. Quitmann, D. Andrich, C. Jarchow, M. Fleuster, B. Beschoten, G. Guntherodt, V.V. Moshchalkov, G. Mante, R. Manzke, Phys. Rev. B **46**, 11813 (1992)
22. M. Covington, L.H. Greene, Phys. Rev. B **62**, 12440 (2000)
23. Y. Takano, S. Takayanagi, S. Ogawa, T. Yamadaya, N. Mori, Solid State Commun. **103**, 215 (1997)
24. W. Jiang, J.L. Peng, J.J. Hamilton, R.L. Greene, Phys. Rev. B **49**, 690 (1994)
25. M.W. Coffey, J.R. Clem, Phys. Rev. Lett. **67**, 368 (1991); M.W. Coffey, J.R. Clem, Phys. Rev. B **46**, 11757 (1992)
26. H.L. Liu, A. Zibold, D.B. Tanner, Y.J. Wang, M.J. Burns, K.A. Delin, M.Y. Li, M.K. Wu, Solid State Commun. **109**, 7 (1999)
27. Z. Yamani, M. Akhavan, Supercond. Sci. Technol. **10**, 427 (1997)
28. D.B. Wiles, R.A. Young, J. Appl. Cryst. **14**, 149 (1981)
29. R.A. Young, in: *The Rietveld Method*, edited by R.A. Young (Oxford University Press, New York, 1993), p. 1
30. Ch. Bertrand, Ph. Galez, R.E. Gladyshevskii, J.L. Jorda, Physica C **321**, 151 (1999)
31. M. Izumi, T. Yabe, T. Wada, A. Maeda, K. Uchinokura, S. Tanaka, H. Asano, Phys. Rev. B **40**, 6771 (1989)
32. K. Koyama, T. Tange, T. Saito, K. Mizuno, Physica B **281&282**, 909 (2000)
33. Z. Klencsar, E. Kuzmann, Z. Homonnay, A. Vertes, K. Vad, J. Bankuti, T. Racz, M. Bodogh, I. Kotsis, Physica C **304**, 124 (1998)
34. D. Wagener, M. Buchgeister, W. Hiller, S.M. Hosseini, K. Kopitzki, Supercond. Sci. Technol. **4**, S211 (1991)
35. L. Colonescu, F. Cairon, J. Berthon, I. Zelenay, R. Suryanarayanan, Physica B **259-261**, 528 (1999)
36. V.N. Narozhnyi, D. Eckert, K.A. Nenkov, G. Fuchs, K.-H. Muller, T.G. Uvarova, `cond-mat/9909107`
37. Z. Zou, Y. Nishihara, Phys. Rev. Lett. **82**, 462 (1999)
38. M. Akhavan, Physica C **250**, 25 (1995)
39. Z. Yamani, M. Akhavan, Physica C **268**, 78 (1996)
40. J.D. Jorgensen, B.W. Veal, A.P. Paulikas, L.J. Nowicki, G.W. Crabtree, H. Claus, W.K. Kwok, Phys. Rev. B **41**, 1863 (1990)
41. M.R. Mohammadizadeh, M. Akhavan, Eur. Phys. J. B **33**, 381 (2003)
42. H. Khosroabadi, M. Modarreszadeh, P. Taheri, M. Akhavan, Phys. Stat. Sol. (c) **1**, 1867 (2004)
43. N.F. Mott, E.A. Davis, *Electronic Processes in Non-crystalline Materials*, 2nd edn. (Clarendon, Oxford, 1979); B.I. Shklovskii, A.L. Efros, *Electronic Properties of Doped Semiconductors*, edited by M. Cardona, P. Fulde, H.-J. Queisser (Springer-Verlag, Berlin, 1984)
44. P.B. Littlewood, C.M. Varma, Phys. Rev. B **45**, 12636 (1992)
45. W.-H. Jung, Physica B **304**, 75 (2001)
46. U. Kabasawa, Y. Tarutani, M. Okamoto, T. Fukazawa, A. Tsukamoto, M. Hiratani, K. Takagi, Phys. Rev. Lett. **70**, 1700 (1993)
47. S.J. Liu, W. Guan, Phys. Rev. B **58**, 11716 (1998)
48. Z. Yamani, M. Akhavan, Solid State Commun. **107**, 197 (1998)
49. H. Khosroabadi, V. Daadmehr, M. Akhavan, Mod. Phys. Lett. B **16**, 943 (2002)
50. M.R. Mohammadizadeh, M. Akhavan, Physica B **336**, 410 (2003)
51. W.H. Tang, J. Gao, J. Phys.: Condens. Matter **11**, 8555 (1999)
52. M.R. Mohammadizadeh, M. Akhavan, Supercond. Sci. Technol. **16**, 1216 (2003)
53. M.R. Mohammadizadeh, M. Akhavan, Supercond. Sci. Technol. **16**, 538 (2003)
54. V. Ambegaokar, B.I. Halperin, Phys. Rev. Lett. **22**, 1364 (1969)
55. J.J. Kim, H.K. Lee, J. Chung, H.J. Shin, H.J. Lee, J.K. Ku, Phys. Rev. B **43**, 2962 (1991)
56. R.H. Koch, V. Foglietti, W.J. Gallagher, G. Koren, A. Gupta, M.P.A. Fisher, Phys. Rev. Lett. **63**, 1511 (1989)
57. Z.H. Wang, S.Y. Ding, Physica C **341-348**, 1247 (2000)
58. T.T.M. Palstra, B. Batlogg, R.B. van Dover, L.F. Schneemeyer, J.V. Waszczak, Phys. Rev. B **41**, 6621 (1990)
59. H. Khosroabadi, V. Daadmehr, M. Akhavan, Iran. J. Phys. Res. **3**, 153 (2002)
60. V. Daadmehr, M. Akhavan, Phys. Stat. Sol. (a) **193**, 153 (2002)
61. L.M. Paulius, C.C. Almasan, M.B. Maple, Phys. Rev. B **47**, 11627 (1993)
62. Y.G. Xiao, B. Yin, J.W. Li, Z.X. Zhao, H.T. Ren, L. Xiao, X.K. Fu, J.A. Xia, Supercond. Science Tech. **7**, 623 (1994)
63. Z.H. Wang, X.W. Cao, Solid State Commun. **109**, 709 (1999)
64. H. Khosroabadi, V. Daadmehr, M. Akhavan, Physica C **384**, 169 (2003)
65. H. Shakeripour, M. Akhavan, Supercond. Sci. Technol. **14**, 234 (2001)
66. J.T. Manscon, J. Giapintzakis, D.M. Ginsberg, Phys. Rev. B **54**, 12517 (1996)
67. C. Li, H. Li, D. Jin, Y. He, G. Xiong, G. Lian, D. Yin, Physica C **341-348**, 2047 (2000)
68. A. Pomar, S.R. Curras, J.A. Veira, F. Vidal, Phys. Rev. B **53**, 8245 (1996)
69. J.S. Moodera, R. Meservey, J.E. Tkaczyk, C.X. Hao, G.A. Gibson, P.M. Tedrow, Phys. Rev. B **37**, 619 (1988)
70. H.S. Gamchi, G.J. Russell, K.N.R. Taylor, Phys. Rev. B **50**, 12950 (1994)
71. B. Oh, K. Char, A.D. Kent, M. Naito, M.R. Beasley, T.H. Geballe, R.H. Hammond, A. Kapitulnik, J.M. Graybeal, Phys. Rev. B **37**, 7861 (1988)
72. H. Shakeripour, M. Akhavan, Iran. J. Phys. Res. **3**, 39, (2002)
73. H. Shakeripour, M. Akhavan, in: *Proceedings of the 1st Regional Conference on Magnetic and Superconducting Materials (MSM-99)*, edited by M. Akhavan, J. Jensen, K. Kitazawa (World Scientific, Singapore, 2000), Vol. A, p. 523
74. D.T. Verebelyi, D.K. Christen, R. Feenstra, C. Cantoni, A. Goyal, D.F. Lee, M. Paranthaman, P.N. Arendt, R.F. Depaula, J.R. Groves, C. Prouteau, Appl. Phys. Lett. **76**, 1755 (2000)